CHARACTERIZING ATMOSPHERIC TURBULENCE FLUCTUATIONS ACROSS SCALES IN THE NORTH ATLANTIC USING SHIPBORNE LIDAR

Rafael Bölsterli
Department of Energy & Process Engineering
Norwegian University of Science & Technology
Trondheim, NO-7491, Norway
rafael.bolsterli@ntnu.no

Felix Kelberlau
Fugro Norway
Trondheim, NO-7462, Norway
f.kelberlau@fugro.com

Yannick Jooss
SINTEF Energy Research
Trondheim, NO-7465, Norway
yannick.jooss@sintef.no

Tania K. Bracchi & R. Jason Hearst
Department of Energy & Process Engineering
Norwegian University of Science & Technology
Trondheim, NO-7491, Norway
jason.hearst@ntnu.no

ABSTRACT

Time-resolved measurements of the open-ocean marine atmospheric boundary layer (MABL) are essential for characterizing the real wind conditions at sea and offer a glimpse into the dynamics of very high Reynolds number unsteady turbulence. A unique dataset obtained using two upward-facing continuous-wave profiling lidars during four trans-Atlantic crossings of a tanker is presented. Horizontal wind velocities were measured by the first lidar between 10 m and 100 m above deck under a wide range of conditions. The vertical profiles indicate that the apparent wind is strongly modified by the vessel and its motions, producing deviations from canonical boundary layer power-law profiles. The second lidar continuously measured at 22 m above deck with an acquisition frequency of roughly 1 Hz to reveal time-resolved results. Velocity increments exhibit sustained heavy-tailed distributions, presumably due to the external intermittency of large flow structures. Two distinct scaling regimes at smaller scales up to 10 s and a second one starting from 1000 s are found. In between the energy spectrum exhibits a robust f^{-1} scaling over nearly two decades, consistent with the attached-eddy model and indicative of very high friction Reynolds numbers $\left(\mathcal{O}\left(10^7\right)\right)$. An active-grid control scheme with constant blockage is implemented to reproduce representative time series in a wind tunnel, accurately reproducing cases with high fidelity.

INTRODUCTION

Vessels travelling at sea experience significant atmospheric turbulence, often assumed to be represented by some form of homogeneous, isotropic turbulence (HIT); but how good is this assumption? For HIT, velocity fluctuations are known to follow quasi-Gaussian distributions (Krogstad & Davidson, 2010). Atmospheric turbulence features strong intermittency, leading to pronounced deviations from Gaussian-like behaviour (Mahrt, 1989). Insights into the intermittency of the flow can be obtained by studying velocity increments $\delta u_\tau(t,\tau)$, defined as the difference between velocity magnitudes measured at times t and $t+\tau$ (Böttcher *et al.*, 2007). From $\delta u_\tau(t,\tau)$, structure functions (moments of order n) can be defined as $S_n(\tau) = \overline{\delta u_\tau(t,\tau)^n}$, which exhibit power-law scaling with the separation τ, i.e. $S_n(\tau) \sim \tau^{\zeta_n}$, where ζ_n denotes the scaling exponent associated with self-similar inertial-range dynamics. This temporal formulation corresponds to the classical spatial scaling under the assumption of Taylor's frozen turbulence hypothesis. Pure self-similarity implies a linear dependence of ζ_n on n, as proposed by Kolmogorov (1941). In this case, the normalized velocity increment PDFs differ only by a scale factor, resulting in a universal distribution independent of the separation τ. However, at sufficiently small separations, no universal PDF shape is observed (Batchelor & Townsend, 1949); instead, the distributions develop heavy tails. This deviation from self-similarity is commonly described by a nonlinear, multifractal scaling behavior, as suggested by Kolmogorov (1962), where the scaling exponent ζ_n becomes a nonlinear function of n with an intermittency correction μ. The resulting heavy-tailed PDFs, characterized by kurtosis values greater than ≈ 3, are commonly referred to as *internal intermittency*.

Nonetheless, heavy-tailed PDFs are frequently found as well in flows with *external intermittency* featuring intermittent or patchy turbulence, as in the outer region of boundary layers. The phenomenon is especially marked in atmospheric boundary layers, where non-turbulent regions extending deep into the flow modulate the turbulence, yielding highly intermittent motions and increased kurtosis (Mahrt, 1989; Böttcher *et al.*, 2007).

A parametrization to describe the shape of PDFs in terms of their deviation from Gaussianity has been proposed by Castaing *et al.* (1990). Based on the log-normal model, the distributions are a superposition of several Gaussian distributions with standard deviations, σ, distributed based on a log-normal distribution. The variance of which determines the shape of the resulting distribution, henceforth referred to as the Castaing parameter, λ_C^2. The Castaing parameter indicates the deviation from Gaussianity, and for the limit of a vanishing λ_C^2, the resulting distribution is again reduced to a single Gaussian. Chillà *et al.* (1996) found a direct way to calculate the Castaing parameter based on the kurtosis of the velocity differences, $K(\delta u_\tau(t,\tau))$,

$$\lambda_C^2(\tau) = \frac{\ln(K(\delta u_\tau(t,\tau))/3)}{4}, \qquad (1)$$

which forms the basis for analysing lidar measurements of the incoming turbulent atmospheric flow. The resulting dataset provides rare open-ocean turbulence statistics beyond coastal sites, allowing a critical examination of their interpretation as intermittency in the measured flow.

DATA ACQUISITION AND PRE-PROCESSING

In early 2025, a 183-meter chemical tanker conducted atmospheric boundary layer measurements while crossing the North Atlantic four times. The campaign consisted of two phases: during the first two legs, measurements were taken with the vessel in its original configuration; for the final two crossings, four 22-meter-high suction-type sails were installed in two pairs on the deck. For all journeys, two collocated ZX300 continuous-wave profiling wind lidars were mounted on the starboard side of the bow, in front of the sails. During each scanning cycle, the lidar focuses on one elevation for one second, then refocuses to scan multiple elevations consecutively. To solve the inherent directional ambiguity of the lidar, two meteorological stations were mounted on the ship. Heading and positional data were obtained using a dual-antenna Global Navigation Satellite System receiver combined with an inertial measurement unit. The first lidar measured vertical wind profiles from 10 m to 38 m in 4 m increments, in addition to a measurement at 100 m above deck. The lidar data were pre-processed in a similar manner as described by Dhomé *et al.* (2025). Because the measurement uncertainty of lidar increases at low apparent wind speeds (AWS), all data from both lidars below 4 m/s were discarded. Vertical profiles from the first lidar were averaged over 10-minute intervals and retained only if at least 15 measurements were available at every height level. Typically, around 30 measurements are recorded for each height in a 10-minute interval. If any height failed to meet this requirement, the entire 10-minute interval was discarded.

The second lidar was set up to measure at 22 m above deck, taking ten samples at 1 Hz before obtaining a reference measurement at 38 m for internal quality control; the latter was not used in the analysis presented here. The resulting dataset contains gaps, both from this measurement sequence and from adverse environmental conditions, which must be filled, as the applied analysis methods require evenly spaced, continuous time series. Therefore, the data is organized into time-series segments, which are defined by data without big gaps; whenever a gap exceeds five minutes, the segment is ended, and a new one is initiated following the gap. The remaining smaller gaps still make up 30% of the data and are filled using a forward- and backward autoregressive scheme as in Yadala *et al.* (2025). The scheme was applied in windows of 1000 s after making sure the window size did not influence the statistics. To verify that the gap-filling did not affect the results, velocity increments were computed, leaving the gaps unfilled, thus excluding all the velocity differences with missing data. A comparison of the probability density functions (PDFs) of velocity increments with and without gap filling showed no observable differences.

Velocity fluctuations are obtained by Reynolds-decomposing the 1 Hz time series with the 10−minute average. The 10−minute average also defines the mean wind direction, which serves as the reference frame for decomposing the velocity into two components: u, aligned with the mean wind direction, and v, perpendicular to it in the horizontal plane. An overbar denotes the temporal averages.

VERTICAL PROFILES OF HORIZONTAL WIND AND TURBULENCE

The measured flow characteristics with and without sails are shown as vertical profiles of AWS in Fig. 1. These profiles represent averages over either the first two or the last two crossings, distinguished by line style. Data is binned into apparent wind angle (AWA) intervals of 30°, and the profiles are normalized with the average at 100 m above the deck. Above the profiles, the number of ensembles for a whole profile is shown. Especially during the first two crossings, almost no data are available for apparent winds from astern, as the ship's forward speed likely often exceeded the wind speed in that direction. Port (left) and starboard (right) profiles at equal apparent wind angles relative to the bow are shown in the same color to make comparisons around the centerline easier. When comparing the measured profiles with boundary-layer profiles based on power-laws, it becomes clear that, especially due to the interaction between the vessel and the flow, there is no one-fits-all solution. As already shown by Wagner *et al.* (2009), even over land, a wide range of velocity profiles can be observed. Using fits of the undisturbed flow, Dhomé *et al.* (2025) also finds a range of power-law exponents, depending on the vessel's position and the possible stability of the atmospheric stratification. Due to limited vertical resolution, fitting boundary-layer profiles is associated with considerable uncertainty. Instead, two reference lines are shown in the figures rather than explicitly estimating power-law exponents. The dotted line indicates the commonly used $1/7$ exponent, while the dash-dotted line represents the modal value (0.035) of the exponent distribution reported by Dhomé *et al.* (2025). The first clearly does not agree with the present findings except for winds from astern, where the wake of the vessel is measured. The latter does agree better, especially for bow-in flows from starboard, where the profiles are almost straight.

Nonetheless, it is clear that the typical boundary layer profiles associated with offshore flows used in simulations and laboratory settings are not realised in these four crossings.

INTERMITTENCY ANALYSIS

In Fig. 2, the Castaing parameter using Eq. (1) for the velocity magnitude of the lidar dataset is compared to a hot-wire (HW) measurement in an approximate HIT generated by an active grid. The grid turbulence measurements were conducted in the wind tunnel of the Norwegian University of Science and Technology; a detailed description of the facility is provided in Kildal *et al.* (2023). The turbulence level was set to roughly match the average turbulence intensity reported by the lidar on all four crossings. Measurements were taken by a Dantec 55P11 single hot-wire probe with a sampling frequency of 75 kHz (see Couliou *et al.*, 2026, for further information). For the HW dataset, the integral time scale, T, is calculated by integrating the autocorrelation up to the first zero-crossing.

As the time lag increases, the Castaing parameter decreases towards zero for both datasets, indicating a shift from heavy-tailed distributions to near-Gaussian ones. As remarked by Renner *et al.* (2001), scale-independent, Gaussian distributions are found for scales larger than T, which is the case for the HW dataset, where λ_C^2 is zero. For the smallest scales

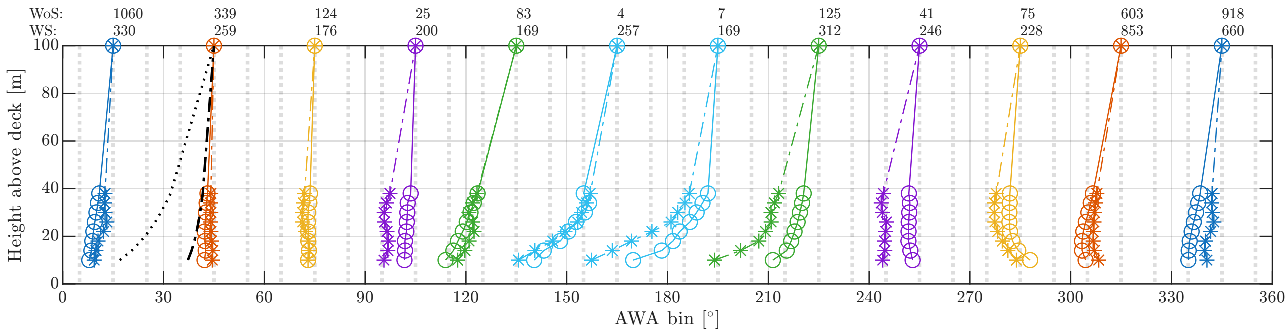

Figure 1: Apparent horizontal wind speed binned into 30° bins with sails (WS) and without them (WoS). The numbers above the profiles indicate the number of ensembles making up a profile. Journeys without sails are shown with solid lines, and dash-dotted with the sails mounted to the vessel. The black profiles show idealized power-laws with an exponent of 0.14 (dotted) and 0.035 (dash-dotted). The minor grid has a spacing of 0.1.

the lidar can resolve, the Castaing parameter is almost double the values of the smallest scales of the HW dataset. While λ_c^2 in the lidar dataset decays to zero at time lags in the order of $\mathscr{O}\left(10^4\right)$ seconds, the time lags for the same in the HW dataset are five orders of magnitude smaller. The slope of the Castaing parameter itself is related to the intermittency correction μ through:

$$\lambda_C^2(\tau) = \left(\Lambda_0^2 - \mu \ln(\tau)\right)/9 \qquad (2)$$

Where Λ_0^2 depends on the macrostructure of the flow (Kolmogorov, 1962; Castaing *et al.*, 1990).

The decay of λ_C^2 in Fig. 2a shows interesting behaviour as the parameter initially drops from almost 0.4 to a plateau spanning roughly two decades of scales. Scales in this plateau, therefore, are self-similar with a linear scaling exponent as the slope of λ_C^2 is close to zero. As a result, the shape of the velocity increment PDF is only scaled and not changed. Only after a time lag of 1000 s, λ_C^2 starts to drop to zero. The yellow and blue lines in Fig. 2a show a regime, where a f^{-1} scaling is found in the energy spectrum, see section below. Note that the bounds of the scaling behavior do line up with the regime of a constant Castaing parameter. Similar shapes of the Castaing parameter as displayed in the lidar dataset have also been reported, for instance, by Neuhaus *et al.* (2020), at 40 meshwidths downstream of the active turbulence grid. The flow seemed to be influenced by two scales, producing a plateau in the Castaing parameter as well. In another study using data sampled over a long period at the FINO1 platform in the North Sea, a slightly different measure was used for the shape of the resulting velocity increments. In their study, Sim *et al.* (2024) calculated the velocity increment distributions as a function of the separation distance by applying Taylor's hypothesis of frozen turbulence, using the local average velocity to convert time lags into spatial separations. The resulting PDFs were fit by skewed and stretched exponential functions, indicating the decay of the tails of a distribution. The tails of the distributions altered as well in two steps, with a plateau in between. A first change to the PDF shape is found up to separations between 0.1 km and 1 km, followed by a constant shape up to separations of more than 10 km, before the PDFs become more and more Gaussian. A very similar behavior with transitions at similar separations is found for the present dataset, where the separation distance is calculated using the local mean velocity for Taylor's hypothesis (not shown here). Such behavior may be an intrinsic feature of atmospheric turbulence, in which two

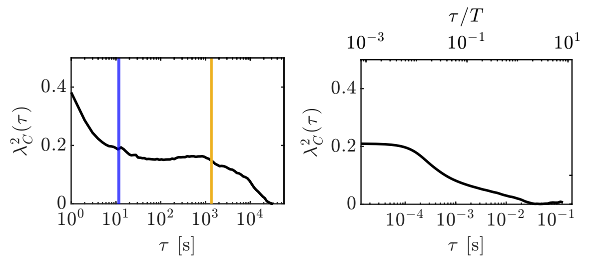

(a) (b)

Figure 2: (a) Castaing parameter as a function of time lag, τ in seconds. The yellow and blue lines show the start and end of a regime where the power spectrum follows a f^{-1} scaling. (b) Castaing parameter for approximately homogeneous turbulence behind an active grid as a function of temporal separation in seconds, as well as normalized by T in the upper axis.

dominant scales govern the flow field: a local scale up to about 0.1 km, and a larger-scale regime beyond 10 km. In the temporal domain, the local scales seem to act on scales shorter than 10 s, whereas the larger scales are found at time scales larger than 1000 s.

Plotting the PDF of velocity increments reveals the change in their shape for different time scales captured by the Castaing parameter. Again, the lidar data is compared to the same HW data in Fig. 3. For each plotted PDF, λ_C^2 is calculated using Eq. (1) and fed into the symmetrical distribution introduced by Castaing *et al.* (1990) and plotted in dashed lines.

For the lidar dataset, the PDFs are heavy-tailed up to the very largest scales. The second and third PDFs ($\tau =$ 60 s and 600 s) are very similar in shape as they both are in the regime where the Castaing parameter is nearly constant. Comparing both laboratory and atmospheric flows as well, Böttcher *et al.* (2007) shows the same heavy-tailed PDFs for atmospheric conditions as found with the present datasets.

SPECTRAL ANALYSIS

The power spectrum of the velocity fluctuations at 22 m above deck, sampled at 1 Hz and computed using Welch's method over all journeys and incident AWA for both velocity components, is shown in light blue in Fig. 4. A moving aver-

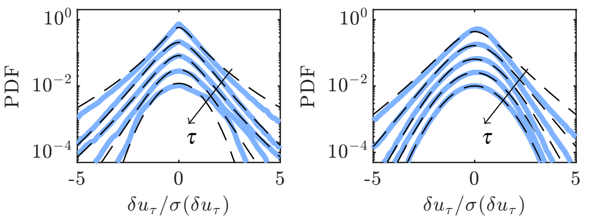

(a) (b)

Figure 3: (a) Normalized probability density functions for different time lags $\tau = 1, 60, 600, 1000, 30000$ s from top to bottom of the measured velocity increments in blue. Curves are shifted for clarity. Black dashed curves are Castaing distributions with the corresponding λ_C^2 values using Eq. (1). (b) Shows distributions of the lab dataset with a time lag of $\tau/T = 0.01$, 0.06, 0.6, 1, 6.

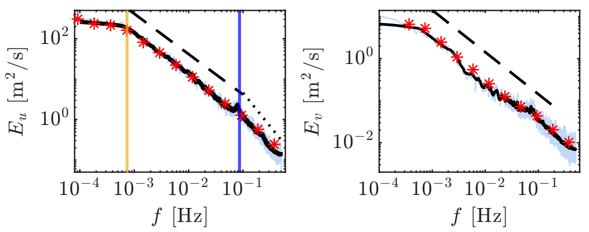

(a) (b)

Figure 4: (a) Energy spectrum of the u velocity component. (b) Spectrum of the velocity component v, perpendicular to the mean wind direction. The black dashed line shows a f^{-1} scaling while the dotted line in (a) shows a $f^{-5/3}$ scaling law. Red markers show the energy density determined by OWTs.

age with a logarithmically increasing window size is applied to obtain the smoothed curves shown as a continuous black line. In addition, orthonormal wavelet transforms (OWT) using a Haar mother wavelet are indicated by the red markers. OWTs are frequently employed in the context of scaling laws in the atmospheric boundary layer, as they are less sensitive to non-stationarities in the velocity time series compared to a Fourier-based analysis (Katul *et al.*, 2012; Banerjee & Katul, 2013). As predicted by the attached eddy model (AEM), the energy spectrum of the streamwise component does follow f^{-1} scaling, before a scaling according to Kolmogorov (1941) of $f^{-5/3}$ is found for higher frequencies (Perry & Abell, 1977; Perry & Chong, 1982). Similar to other studies, E_u does follow the f^{-1} slope better than E_v (Banerjee & Katul, 2013; Liu *et al.*, 2022). The spectrum of the u component exhibits an f^{-1} scaling across almost two decades, which is among the longest ranges reported to the authors' knowledge (Calaf *et al.*, 2013; Liu *et al.*, 2022). The beginning and ending of the range, where the AEM scaling is found, are indicated by the yellow and blue lines in the same way in all Figs. 2a,4a, and 5. Especially for E_u, an energy built up is noticeable at around 0.1 Hz, which is likely due to the reference measurements of the lidar: As the lidar has to refocus its optics from 22 m to 32 m and vice-versa, the measurements after refocusing are not spaced exactly one second apart. As measurements are only provided with timestamps rounded to the closest second, this temporal discrepancy cannot be adjusted. As E_v is generally noisier, the peak is less profound.

Using a least square fit for frequencies between 7.3×10^{-4} Hz to 0.07 Hz indicates scalings of f^{-1} for the unsmoothed Fourier-based spectral density and $f^{-0.95}$ for the OWT. Following the argumentation of Katul *et al.* (2012), the scaling should be corrected and shallower for intermittent cases. Specifically, a correction using μ is proposed, thus a scaling of $f^{-1+\mu}$ should be recovered. As discussed in the previous section, the Castaing parameter is constant for the regime, where the f^{-1} scaling is found, thus μ is zero for this regime as well, resulting in an uncorrected scaling law. It should, however, be noted that the flow field still shows heavy tails in the distribution, which might be an indication of very large motions interacting with the flow.

To transfer the spectrum into wave number space, Taylor's hypothesis of frozen turbulence is used, whereby the velocity average was taken for each time series separately. It is known that this transformation is plagued with problems in the boundary and shear layers (Álamo & Jiménez, 2009; Moin, 2009). Similar to other studies in the ABL, the interest here lies in rather large wave numbers, where Taylor's hypothesis should hold reasonably well (Kunkel & Marusic, 2006; Calaf *et al.*, 2013; Sim *et al.*, 2023).

Using the same range as above, the wave-number spectrum can be fit as $E_u(k) = C'_{TKE} U_*^2 k^{-1}$ (Banerjee & Katul, 2013), yielding an estimate of the friction velocity, U_*, where the constant C'_{TKE} is observed between $0.9 - 1.1$ according to multiple measurements in the atmosphere (Banerjee & Katul, 2013). U_* is found in a range between 0.26 m/s $- 0.29$ m/s. As the extent of the scaling law indicates very large friction Reynolds numbers, Re_*, an estimate is made using a MABL height of around 1 km (Zhou *et al.*, 2020; Yang & Pan, 2025). Using tabulated values from the international standard atmosphere for the kinematic viscosity of air, Re_* is found in the order of $\mathcal{O}(10^7)$. As comparison, a boundary layer with a f^{-1} scaling for less than a decade requires a friction Reynolds number of order $\mathcal{O}(10^5)$ (Marusic & Monty, 2019).

In Fig. 5, the premultiplied spectrum is normalized using the fitted friction velocity and the measurement height above the sea surface, z, which changed with vessel loading and sea state. As the change to the result from the two extreme normalizations of maximum and minimum draft (9 m to 13 m) is not significant, an intermediate lidar height is used, resulting in a measurement height of 34 m above the sea surface. In the premultiplied and normalized spectrum, a k^{-1} scaling is expected as a horizontal line at unity.

The transition between the k^{-1} scaling and the $k^{-5/3}$ scaling of the intermediate scales is believed to happen at a constant kz. Many studies have found the transition at roughly unity (Kunkel & Marusic, 2006; Katul *et al.*, 2012; Calaf *et al.*, 2013). The transition in Fig. 5 is found at slightly higher wave numbers of $kz \approx 1.6$; however, the transition is difficult to distinguish due to the peak originating from the time uncertainty. In other measurements of the MABL, Liu *et al.* (2022) found the transition at higher wave numbers (up to $kz \approx 3.4$) for wind-following swell conditions. Sim *et al.* (2023) showed the transition at $kz \approx 2$

In the premultiplied spectra of Sim *et al.* (2023), the energy does increase at the lower wavenumber bond of the k^{-1} scaling, possibly an imprint of gravity-waves, which is not found with this data-set. Rather, a scaling close to k^0 is found, in the premultiplied spectrum visible with a slope of $+1$. According to Nikora (1999), the onset of this scaling is found at $kH \leq 1$, where H is the external length scale of the flow proportional to the boundary layer thickness. Inserting the end of

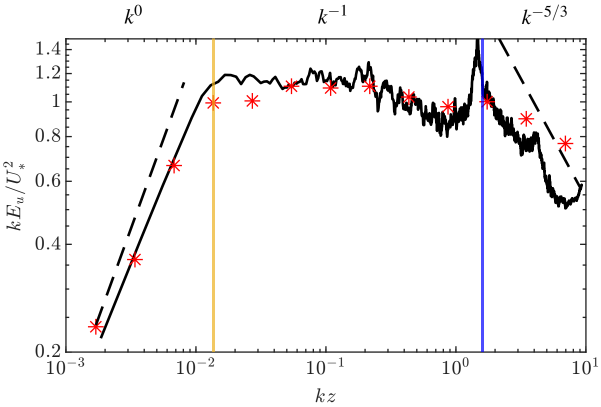

Figure 5: Premultiplied spectrum from Fig. 4a plotted in wavenumber space and normalized with the measurement height as well as the friction velocity. The yellow and blue lines show the approximate transition points of the different scalings, indicated by the dashed lines.

the f^{-1} scaling at $kz = 0.014$ gives $H = 15.6$ km. The end of the f^{-1} scaling in Calaf *et al.* (2013) appears at approximately the same value of normalized wave number kz.

REPRESENTATIVE TIME SERIES AND THEIR EXPERIMENTAL REPLICATION

Ten representative time-series are extracted from the data set for replication and investigation in the lab and simulations.

To enable reliable reproduction of the selected time series, an active-grid control scheme is implemented. The approach builds on the method developed at the University of Oldenburg, in which the global blockage of the grid is maintained constant, and lidar-based velocity measurements have been successfully reproduced in a wind tunnel (Kröger *et al.*, 2018; Neuhaus *et al.*, 2021).

The actuation principle is based on controlling the flap angle of the active grid between 0° (fully open) and 90° (maximum blockage), with the flaps undergoing a prescribed back-and-forth motion rather than continuous rotation. Adjacent shafts rotate in opposite directions to avoid inducing a mean flow deflection, thereby generating an array of small jets with a controllable effective opening.

To avoid excessive loading of the wind tunnel fan, the overall grid blockage is kept constant. This is achieved by assigning the 90 actuators to two groups. The first group, denoted A, actively follows the prescribed time-dependent signal, while the second group, C, compensates for these motions such that the total blockage remains constant. Different combinations of shaft groups (A, C) are used to impose the prescribed signal at different spatial locations. Effective compensation requires the compensating group to provide a larger blockage contribution than the active group. As the grid is not square, this constraint does not directly correspond to the number of actuators, but rather to their effective blockage.

To establish the relationship between shaft angle and flow velocity, a transfer function is measured. This procedure is repeated for each shaft-group configuration, undisturbed (fully open grid) flow velocity, and measurement location. For a given case, the wind tunnel is first set to the desired undisturbed flow velocity. The shafts in group A are then set to 90° (fully closed), while group C remains open to maintain constant blockage. The resulting flow velocity is recorded at the

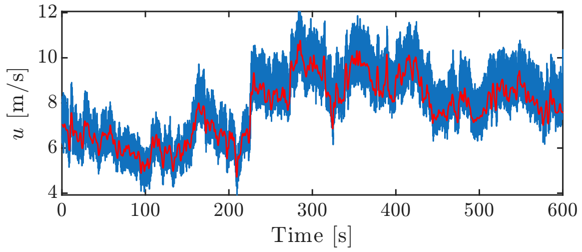

Figure 6: Comparison between the prescribed input and the reproduced time series in the wind tunnel. The downsampled HW signal in blue is shown against the input signal in red.

measurement location over 3 min. Subsequently, the angle of group A is reduced in increments of 3°, with group C adjusted accordingly to preserve constant blockage. At each step, the flow velocity is measured. This process continues until group A is fully open and group C is fully closed. The resulting measurements are then fit with an eighth-degree polynomial, yielding the transfer function.

For the initial results shown above, the active grid is split horizontally in the middle, to have the active group at the lower half and the compensation group at the upper half. The flow velocity with the active grid fully opened is 10 m/s, and the measurement location is 3 m or 30 grid mesh lengths, M, downstream of the active grid and 30.7 cm above the tunnel floor. After determining the transfer function, a test signal measured by the lidar in the Atlantic (red line in Fig. 6) is fed into the control scheme. As indicated by the downsampled 75 kHz HW measurement (blue), the time series is captured well, with a coefficient of determination of $R^2 = 0.96$, demonstrating a high level of agreement.

CONCLUSIONS

Onboard measurements of horizontal wind using two upward-facing lidars provided unprecedented data on the MABL in the North Atlantic. Measurements were performed on four trans-Atlantic crossings. One lidar measured vertical profiles of elevations from 10 m up to 100 m above the deck of a tanker. Datapoints are averaged over 10 min and grouped into 30° bins to show the influence of the vessel and wind direction. The horizontal apparent wind is dominated by flow modifications induced by the vessel, which prevents the definition of a meaningful mean behaviour.

The second lidar focused on an elevation of 22 m above deck at a temporal resolution of roughly 1 Hz. By assessing the distributions of velocity increments across scales using the Castaing parameter, two regimes with enhanced internal intermittency are found. One with scales up to 10 s, a second one for scales larger than 1000 s. In between the Castaing parameter shows almost a constant value of 0.2, still indicating heavy-tailed PDFs, which is also found when plotting them. Comparing that with HIT from wind tunnel measurements downstream of an active turbulence grid displays the large difference in scales, as well as no intermediate plateau of the Castaing parameter for HIT data. In the range where the Castaing parameter remains approximately constant, the spectrum follows an f^{-1} scaling, consistent with predictions from the AEM. The broad extent of this scaling region suggests a substantial friction Reynolds number, on the order of $\mathcal{O}\left(10^7\right)$. Although the observed heavy-tailed increment distributions clearly reflect interactions with large-scale or mesoscale motions, the constancy of the Castaing parameter implies no need for intermittency correction to the f^{-1} scaling. Intermittency is formally defined through deviations of the structure-function exponents ζ_n from linearity in the moment order n. Heavy tails are, therefore, necessary but not sufficient to establish internal intermittency. The results indicate that open-ocean atmospheric turbulence departs from canonical near-Gaussian statistics with an increased occurrence of strong events.

In addition, a constant-blockage actuation scheme is implemented using an active grid in a wind tunnel, enabling controlled reproduction of the selected inflow conditions. The results demonstrate good agreement between the prescribed input and the measured velocity signal, confirming the capability of the approach to replicate realistic atmospheric inflow features under laboratory conditions.

ACKNOWLEDGEMENTS

This work was partly funded by the Research Council of Norway (reSail - Sailing with wind-assisted propulsion in realistic wind conditions, 353095). The views and opinions expressed are those of the author(s) only and do not necessarily reflect those of the Research Council of Norway. Neither the Research Council nor the granting authority can be held responsible for them.

REFERENCES

Álamo, J.C.D. & Jiménez, J. 2009 Estimation of turbulent convection velocities and corrections to Taylor's approximation. *J. Fluid Mech.* **640**, 5–26.

Banerjee, T. & Katul, G.G. 2013 Logarithmic scaling in the longitudinal velocity variance explained by a spectral budget. *Phys. Fluids* **25** (12), 125106.

Batchelor, G.K. & Townsend, A.A. 1949 The nature of turbulent motion at large wave-numbers. *Proc. R. Soc. A* .

Böttcher, F., Barth, S. & Peinke, J. 2007 Small and large scale fluctuations in atmospheric wind speeds. *Stoch Environ Res Ris Assess* **21** (3), 299–308.

Calaf, M., Hultmark, M., Oldroyd, H.J., Simeonov, V. & Parlange, M.B. 2013 Coherent structures and the k^{-1} spectral behaviour. *Phys. Fluids* **25** (12), 125107.

Castaing, B., Gagne, Y. & Hopfinger, E.J. 1990 Velocity probability density functions of high Reynolds number turbulence. *Physica D: Nonlinear Phenomena* **46** (2), 177–200.

Chillà, F., Peinke, J. & Castaing, B. 1996 Multiplicative process in turbulent velocity statistics: a simplified analysis. *J. Phys. II France* **6** (4), 455–460.

Couliou, M., Yadala, S., Jankee, G.K., Neunaber, I. & Hearst, R.J. 2026 The effect of freestream turbulence on wing-tip vortex meandering and deformation. *Int. J. Heat Fluid Flow* **117**, 110013.

Dhomé, U., Kuttenkeuler, J. & Segalini, A. 2025 Observation of the atmospheric boundary layer over the Atlantic and its effects for wind propulsion. *J. Wind Eng. Ind. Aerodyn.* **258**, 106014.

Katul, G.G., Porporato, A. & Nikora, V. 2012 Existence of k^{-1} power-law scaling in the equilibrium regions of wall-bounded turbulence explained by Heisenberg's eddy viscosity. *Phys. Rev. E* **86** (6), 066311.

Kildal, O., Li, L., Hearst, R.J., Petersen, Ø.W. & Øiseth, O. 2023 On the use of an active turbulence grid in wind tunnel testing of bridge decks. *J. Wind Eng. Ind. Aerodyn.* **233**, 105331.

Kolmogorov, A.N. 1941 The local structure of turbulence in incompressible viscous fluid for very large Reynolds numbers. *Dokl. Akad Nauk SSSR* **31**, 301–305.

Kolmogorov, A.N. 1962 A refinement of previous hypotheses concerning the local structure of turbulence in a viscous incompressible fluid at high Reynolds number. *J. Fluid Mech.* **13** (1), 82–85.

Kröger, L., Frederik, J., van Wingerden, J.-W., Peinke, J. & Hölling, M. 2018 Generation of user defined turbulent inflow conditions by an active grid for validation experiments. *J. Phys.: Conf. Ser.* **1037** (5), 052002.

Krogstad, P.-Å. & Davidson, P.A. 2010 Is grid turbulence Saffman turbulence? *J. Fluid Mech.* **642**, 373–394.

Kunkel, G.J. & Marusic, I. 2006 Study of the near-wall-turbulent region of the high-Reynolds-number boundary layer using an atmospheric flow. *J. Fluid Mech.* **548**, 375–402.

Liu, C., Li, X., Song, J., Zou, Z., Huang, J., Zhang, J.A., Jie, G. & Wang, J. 2022 Characteristics of the marine atmospheric boundary layer under the influence of ocean surface waves. *J. Phys. Oceanogr* **52** (6), 1261–1276.

Mahrt, L. 1989 Intermittency of atmospheric turbulence. *J. Atmos. Sci.* **46** (1), 79–95.

Marusic, I. & Monty, J.P. 2019 Attached eddy model of wall turbulence. *Annu. Rev. Fluid Mech.* **51** (1), 49–74.

Moin, P. 2009 Revisiting Taylor's hypothesis. *J. Fluid Mech.* **640**, 1–4.

Neuhaus, L., Berger, F., Peinke, J. & Hölling, M. 2021 Exploring the capabilities of active grids. *Exp. Fluids.* **62** (6), 130.

Neuhaus, L., Hölling, M., Bos, W.J. T. & Peinke, J. 2020 Generation of atmospheric turbulence with unprecedentedly large Reynolds number in a wind tunnel. *Phys. Rev. Lett.* **125** (15), 154503.

Nikora, V. 1999 Origin of the "-1" spectral law in wall-bounded turbulence. *Phys. Rev. Lett.* **83** (4), 734–736.

Perry, A.E. & Abell, C.J. 1977 Asymptotic similarity of turbulence structures in smooth- and rough-walled pipes. *J. Fluid Mech.* **79** (4), 785–799.

Perry, A.E. & Chong, M.S. 1982 On the mechanism of wall turbulence. *J. Fluid Mech.* **119**, 173–217.

Renner, C., Peinke, J. & Friedrich, R. 2001 Experimental indications for Markov properties of small-scale turbulence. *J. Fluid Mech.* **433**, 383–409.

Sim, S.-K., Maass, P. & Roman, H. E. 2024 Distributions and correlation properties of offshore wind speeds and wind speed increments. *Bound.-Layer Meteorol.* **190** (11), 48.

Sim, S.-K., Peinke, J. & Maass, P. 2023 Signatures of geostrophic turbulence in power spectra and third-order structure function of offshore wind speed fluctuations. *Sci Rep* **13** (1), 13411.

Wagner, R., Antoniou, I., Pedersen, S.M., Courtney, M.S. & Jørgensen, H.E. 2009 The influence of the wind speed profile on wind turbine performance measurements. *Wind Energy* **12** (4), 348–362.

Yadala, S., Dehareng, S., Neunaber, I., Jankee, G.K., Kaufmann, R., Couliou, M. & Hearst, R.J. 2025 The effect of turbulence on a flexible finite wing: forces, deflections and the wingtip vortex. *J. Fluid Mech.* **1019**, A38.

Yang, S.-S. & Pan, C.-J. 2025 Climatology of the atmospheric boundary layer height using ERA5: spatio-temporal variations and controlling factors. *Atmosphere* **16** (5), 573.

Zhou, J., Xiang, J. & Huang, S. 2020 Marine boundary layer height obtained by new numerical regularization method based on GPS radio occultation data. *Sensors* **20** (17), 4762.